Nano-Micro Letters
COMMUNICATION
ISSN 2311-6706
e-ISSN 2150-5551
CN 31-2103/TB
https://doi.org/10.1007/s40820-019-0312-y

Cite as
Nano-Micro Lett.
(2019) 11:81

Received: 11 August 2019
Accepted: 1 September 2019
Published online: 25 September 2019

Plate-to-Layer Bi_2MoO_6/MXene-Heterostructured Anode for Lithium-Ion Batteries

Peng Zhang[1], Danjun Wang[1,2], Qizhen Zhu[1] ✉, Ning Sun[1], Feng Fu[2] ✉, Bin Xu[1] ✉

✉ Qizhen Zhu, zhuqz@mail.buct.edu.cn; Feng Fu, yadxfufeng@126.com; Bin Xu, binxumail@163.com

[1] State Key Laboratory of Organic-Inorganic Composites, Beijing Key Laboratory of Electrochemical Process and Technology for Materials, Beijing University of Chemical Technology, Beijing 100029, People's Republic of China

[2] Shaanxi Key Laboratory of Chemical Reaction Engineering, School of Chemistry and Chemical Engineering, Yan'an University, Yan'an 716000, People's Republic of China

HIGHLIGHTS

- The highly conductive $Ti_3C_2T_x$ (MXene) is introduced as a substrate for loading Bi_2MoO_6.
- The Bi_2MoO_6/MXene heterostructure exhibits ultra-long cycle durability and superior rate capability.
- Electrochemical kinetic mechanism is analyzed for the as-prepared heterostructure.

ABSTRACT Bi_2MoO_6 is a potentially promising anode material for lithium-ion batteries (LIBs) on account of its high theoretical capacity coupled with low desertion potential. Due to low conductivity and large volume expansion/contraction during charge/discharge cycling of Bi_2MoO_6, effective modification is indispensable to address these issues. In this study, a plate-to-layer Bi_2MoO_6/$Ti_3C_2T_x$ (MXene) heterostructure is proposed by electrostatic assembling positive-charged Bi_2MoO_6 nanoplates on negative-charged MXene nanosheets. MXene nanosheets in the heterostructure act as a highly conductive substrate to load and anchor the Bi_2MoO_6 nanoplates, so as to improve electronic conductivity and structural stability. When the mass ratio of MXene is optimized to 30%, the Bi_2MoO_6/MXene heterostructure exhibits high specific capacities of 692 mAh g^{-1} at 100 mA g^{-1} after 200 cycles and 545.1 mAh g^{-1} with 99.6% coulombic efficiency at 1 A g^{-1} after 1000 cycles. The results provide not only a high-performance lithium storage material, but also an effective strategy that could address the intrinsic issues of various transition metal oxides by anchoring them on MXene nanosheets to form heterostructures and use as anode materials for LIBs.

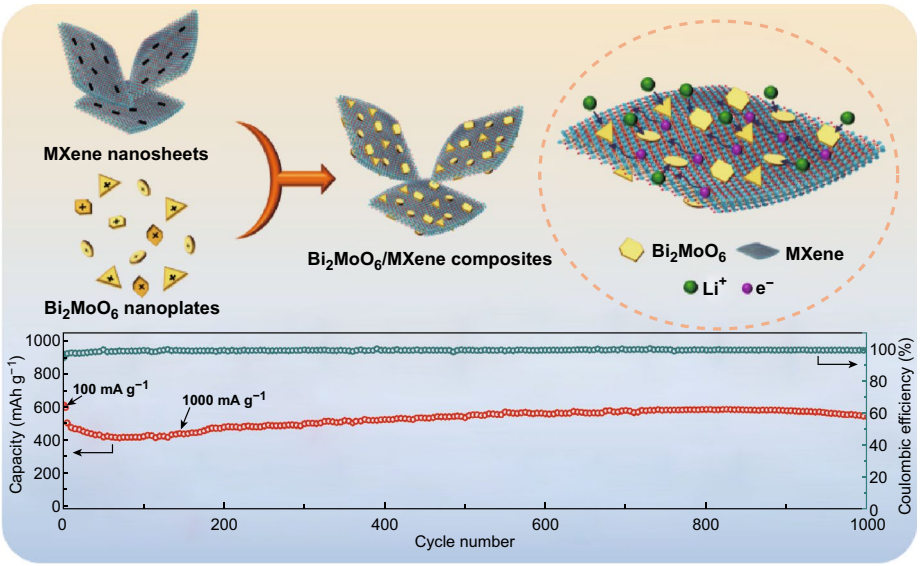

KEYWORDS Bi_2MoO_6; MXene; Electrostatic self-assembly; Heterostructure; Lithium-ion batteries

1 Introduction

Lithium-ion batteries (LIBs), with advantages of high energy density, environmental benignity, and no memory effect, have occupied unparalleled markets of electric vehicles and portable electronics [1–3]. However, the low theoretical capacity (372 mAh g^{-1}) of the commercial graphite anode material actually limits the further development of LIBs due to the booming demand for higher energy density in applications, which urges researchers to explore high-performance anode materials for next-generation LIBs [4, 5]. On this account, a variety of transition metal oxides (TMOs) have been investigated as anode materials for LIBs because of their high theoretical capacity and moderate cost [6–8], e.g., SnO_2 [9, 10], Fe_3O_4 [11], and Mn_3O_4 [12]. Nevertheless, owing to their alloying or conversion storage mechanism, the huge volume expansion/contraction of TMOs during lithiation/delithiation processes results in the instability of the electrode structure and the repeated cracking/forming of the solid electrolyte interface (SEI), leading to the capacity fading together with continuous consumption of electrolyte [13–16]. For example, SnO_2 can store up to 4.4 units of Li in one unit of Sn, endowing with a high theoretical capacity of 790 mAh g^{-1} as well as a volume charge of more than 200% [17]. Decreasing the particle size of TMOs to nanoscale coupled with morphological control (e.g., nanotubes [18], nanospheres [19], and nano-flowers [20]) provides a promising direction to improve the cycling stability of TMOs [16, 21, 22]. In addition, the intrinsic low electrical and ionic conductivity renders the TMOs with unacceptable rate capability, which also obstructs its application as electrode material of LIBs [6, 16, 21]. An efficient strategy to overcome this issue is to rationally design composites combining TMOs and highly conductive materials, such as graphene [23], carbon nanotubes [24], and amorphous carbon [25].

Among various TMOs, bismuth molybdate (Bi_2MoO_6) with a structure of alternate $[Bi_2O_2]^{2+}$ layers and $[MoO_4]^{2-}$ perovskite layers can be potentially used as an anode material for LIBs due to its high theoretical capacity (791 mAh g^{-1}) as well as low desertion potential (< 1.0 V) [26, 27]. Up to date, most reports about Bi_2MoO_6 focused on its photocatalyst properties, while its application in LIBs, which has great significance, still needs further development. When used as anode material, the main restricts of Bi_2MoO_6 are similar to those of other TMOs, i.e., the large volume change during lithiation/delithiation and the intrinsic low conductivity. Thus, the strategies of rational design on the structure and combination with conductive materials can also be employed for improving electrochemical performances of Bi_2MoO_6 electrode material [27–31]. For example, Zhai et al. [28] reported a Bi_2MoO_6/reduced graphene oxide (rGO) composite based on the in situ growth of Bi_2MoO_6 on the rGO substrate, in which the rGO provides high conductivity and is beneficial for exposing the active sites and alleviating the volume change of Bi_2MoO_6.

More recently, two-dimensional (2D) transition metal carbides and nitrides known as MXenes have been widely studied because of their high metallic conductivity, tailorable surface chemistries, and mechanical flexibility [32–35]. Typically, MXenes are synthesized by selectively etching the A layer (group IIIA or group IVA element) from the ternary precursors known as MAX phases and have a general formula of $M_{n+1}X_nT_x$, where M is an early transition metal; X stands for C and/or N; $n = 1$, 2, or 3; T_x represents the surface functional groups, such as –O, –F, and –OH [36, 37]. According to the calculation result, $Ti_3C_2T_x$, one of the most studied MXenes possesses lower lithium diffusion barrier (~ 0.07 eV) compared with that of the graphite carbons (~ 0.3 eV), indicating faster Li^+ transport and higher lithiation/delithiation rate than the commercial graphite anode [38, 39]. In this regard, $Ti_3C_2T_x$ MXene could be an ideal substrate to combine with various TMOs (e.g., SnO_2 [40, 41], Fe_3O_4 [42], Sb_2O_3 [43], $LiMn_2O_4$ [44]) to fabricate high-performance electrode materials for LIBs. For example, Zhao et al. [45] fabricated a flexible $Ti_3C_2T_x/NiCo_2O_4$ hybrid film via an in situ growth method. As the $Ti_3C_2T_x$ facilitated fast ion transport and electron transfer, the electrochemical performance of the film electrode was effectively enhanced. Therefore, integrating with the highly conductive $Ti_3C_2T_x$ MXene is expected to significantly improve the lithium storage performances of Bi_2MoO_6.

In this work, for the first time, Bi_2MoO_6/MXene ($Ti_3C_2T_x$) composites with a plate-to-layer heterostructure have been fabricated through a simple electrostatic self-assembly followed by freeze-drying method. Based on the electrostatic interaction, the positive-charged Bi_2MoO_6 nanoplates are

https://doi.org/10.1007/s40820-019-0312-y

uniformly anchored on the surface of the negative-charged MXene nanosheets, leading to a synergistic effect between the Bi_2MoO_6 nanoplates and the MXene nanosheets with several merits: (i) The Bi_2MoO_6 nanoplates distributed on the MXene can sufficiently expose the active sites for high capacity and simultaneously serve as spacers to prevent the MXene nanosheets from restacking, so could greatly enhance the ion accessibility. (ii) The MXene can effectively prevent the Bi_2MoO_6 nanoplates from aggregation and alleviate their huge volume change in lithiation/delithiation processes, effectively avoiding the loss of the active sites and ensuring the cycle stability. (iii) The MXene nanosheets contact closely with the Bi_2MoO_6 nanoplates, which can enhance the electronic conductivity and facilitate Li^+ diffusion, in favor of the rate performance. Consequently, acting as an anode material for LIBs, the Bi_2MoO_6/MXene heterostructures exhibit high capacity, superior rate capability, and excellent cycling stability, demonstrating not only a promising LIBs anode material, but also the effectiveness of MXene substrate in place to enhance the electrochemical performance of TMOs.

2 Experimental

2.1 Materials Syntheses

2.1.1 Synthesis of $Ti_3C_2T_x$ MXene

The MXene nanosheets were obtained as reported previously [40, 46, 47]. Typically, 0.99 g of lithium fluoride (LiF) was added to 10 mL of 12 M hydrochloric acid (HCl) under stirring for dissolving. Then, 1 g of Ti_3AlC_2 powder (400 mesh, purchased from 11 Technology Co. Ltd) was slowly added to the above solution. The mixture was stirred at 35 °C for 24 h to ensure the complete etching. After that, the residue was washed with deionized water for several times until the pH of the supernatant is above 6. The precipitate was then re-dispersed in deionized water followed by sonication for 1 h under Ar atmosphere. After centrifugation at 5200 rpm for 1 h, the supernatant was collected as the MXene aqueous solution. In order to determine the concentration of the MXene aqueous solution, 5 mL of MXene aqueous solution was filtered and vacuum dried to obtain a pristine MXene film. After weighting the film, the concentration was obtained. The concentration of MXene aqueous solution was diluted to 2 mg mL^{-1}.

2.1.2 Synthesis of the Bi_2MoO_6 Nanoplates

The Bi_2MoO_6 nanoplates were synthesized as reported previously [48]. Typically, 2 mmol of $Bi(NO_3)_3{\cdot}5H_2O$ was added to 10 mL of HNO_3, while 0.143 mmol of $(NH_4)_6Mo_7O_{24}{\cdot}4H_2O$ was dissolved in 10 mL of deionized water, respectively. After stirring for 30 min, the $Bi(NO_3)_3{\cdot}5H_2O$ solution was added to the $(NH_4)_6Mo_7O_{24}{\cdot}4H_2O$ solution dropwise under stirring for 60 min. Once approached to pH neutral (adjusted by ammonium hydroxide), the mixture was transferred into a Teflon-lined stainless steel autoclave and then heating at 180 °C for 12 h. Subsequently, the product was washed with deionized water and absolute ethanol for several times and dried under vacuum to obtain the pristine Bi_2MoO_6 nanoplates.

2.1.3 Synthesis of the Bi_2MoO_6/MXene Heterostructures

The composite Bi_2MoO_6/MXene heterostructures were prepared via an electrostatic self-assembly method. The positive-charged Bi_2MoO_6 nanoplates was added to deionized water and sonicated for 30 min to form the Bi_2MoO_6 suspension (1 mg mL^{-1}). Then, the Bi_2MoO_6 suspension was mixed with the MXene solution (1 mg mL^{-1}) under continuous stirring for 30 min with various ratios. The mixture was freeze-dried for 48 h to obtain the Bi_2MoO_6/MXene heterostructures (denoted as Bi_2MoO_6/MXene-x, where x stands for the mass ratio of MXene in the heterostructures).

2.2 Materials Characterization

The morphology of the prepared Bi_2MoO_6, MXene nanosheets, and Bi_2MoO_6/MXene heterostructures was observed through scanning electron microscope (SEM, Hitachi S4800), transmission electron microscope (TEM, Hitachi HT7700), and scanning transmission electron microscopy equipped with energy-dispersive X-ray spectroscopy (EDS) for elemental mapping (STEM, Hitachi HT7700). Zeta potentials were measured by a Marlvern laser particle size analyzer (ZS980). XRD patterns were performed using X'Pert-Pro MPD (PANalytical, the Netherlands) diffractometer with monochromatic Cu Ka radiation ($\lambda = 1.5418$ Å, with scan speed of 4° min^{-1}). Raman spectra were conducted through Raman spectrometer (Renishaw 1000) with a 1 mW He–Ne laser (633 nm) as an irradiation source. XPS analysis was performed by ESCALAB 250

(ThermoFisher Scientific, USA). AFM image was collected using atomic force microscope (Dimension ICON).

2.3 Electrochemical Measurements

All the electrochemical measurements were taken by assembling CR2025 coin-type cells in Ar-filled glove box at room temperature. The working electrodes were fabricated by mixing active materials (Bi_2MoO_6/MXene heterostructures or Bi_2MoO_6) conductive agent (Super-P) and binder (carboxymethylcellulose sodium, CMC) in deionized water with a mass ratio of 70:20:10 followed by coating the mixed slurry onto copper foil. The mass loading of the active materials on the current collector was fixed to 0.8 mg cm^{-2} in order to standardize the test results. Lithium foil, Celgard 3500 membrane, and 1 M $LiPF_6$ in ethylene carbonate (EC)/diethyl carbonate (DEC) (1:1 by volume) with an addition of 5 wt% fluoroethylene carbonate (FEC) were employed as counter electrode, separator, and electrolyte for LIBs, respectively. The amount of electrolyte used in each coin cell is 120 μL. The galvanostatic charge/discharge tests were carried out on Land BT2000 battery tester (Wuhan, China) in the voltage range of 0.01–3 V. Cyclic voltammetry (CV) measurements were taken on the VSP electrochemical workstation (Bio-Logic, France) with a potential window of 0.01–3 V at a scan rate of 0.1 mV s^{-1}. Electrochemical impedance spectroscopy (EIS) was tested in the frequency range of 100 kHz to 0.1 Hz with amplitude of 10 mV. The galvanostatic intermittent titration technique (GITT) was carried out with current pulse (100 mA g^{-1} for LIBs) for 30 min followed by 1 h relaxation on a Land BT2000 battery tester (Wuhan, China). The diffusion coefficients were calculated from the GITT potential profiles according to the Fick's second law with the following Eq. 1:

$$D = \frac{4}{\pi\tau}\left(\frac{m_B V_M}{M_B S}\right)^2\left(\frac{\Delta E_S}{\Delta E_\tau}\right)^2 \quad (1)$$

where τ stands for the duration of current pulse; m_B represents the mass of active material in the pole; V_M and M_B is the molar volume and the molar mass of the active materials, respectively; S is the geometric area of the electrode; ΔE_τ means the potential variation during the current pulse; and ΔE_S represents the quasi-thermodynamic equilibrium potential variation before and after the current pulse.

3 Results and Discussion

Figure 1 illustrates the synthetic process for the Bi_2MoO_6/MXene heterostructure. First, the delaminated $Ti_3C_2T_x$ MXene nanosheets were produced by etching aluminum (Al)

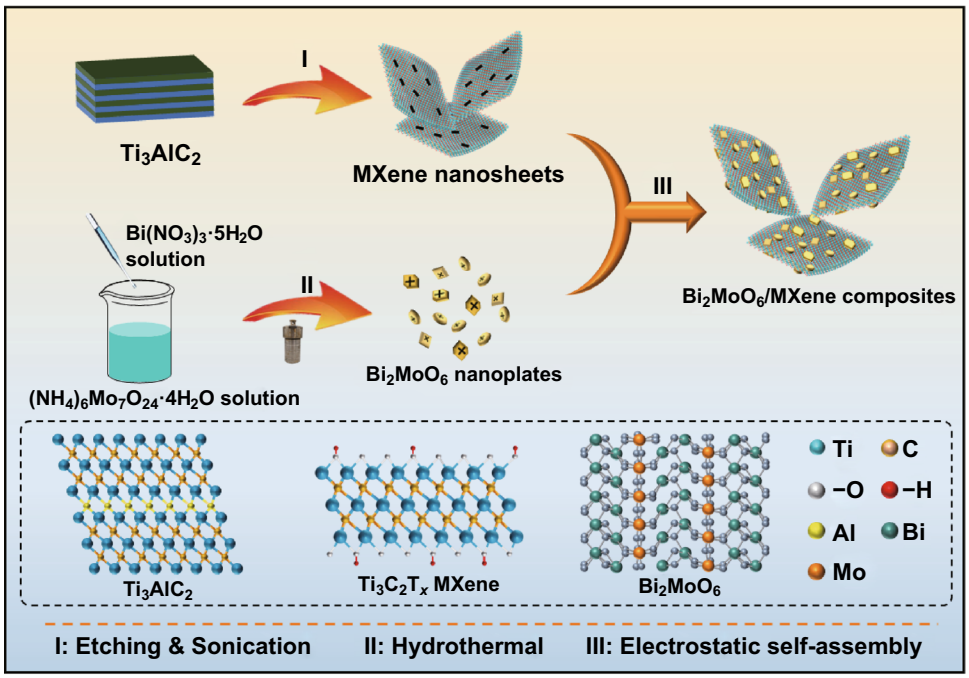

Fig. 1 Schematic diagram for the simple electrostatic self-assembly of positive-charged Bi_2MoO_6 nanoplates on the negative-charged MXene nanosheets

https://doi.org/10.1007/s40820-019-0312-y

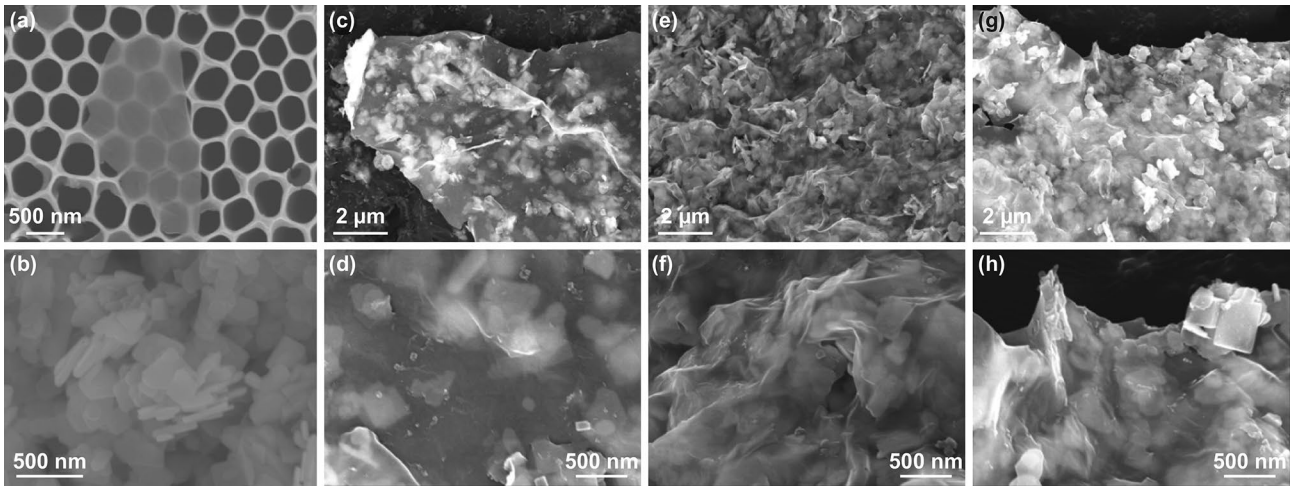

Fig. 2 SEM images of **a** MXene nanosheets, **b** Bi_2MoO_6 nanoplates, **c**, **d** Bi_2MoO_6/MXene-50%, **e**, **f** Bi_2MoO_6/MXene-30%, and **g**, **h** Bi_2MoO_6/MXene-10%

layers from Ti_3AlC_2 precursor with a solution of LiF and HCl, followed by sonication and the subsequent centrifugation. As shown in Fig. S1, the SEM image indicates the Ti_3AlC_2 MAX phase has a layered structure, and the XRD pattern is consistent with that of the previous reports [32, 33]. Single or few-layered MXene nanosheets can be readily obtained through such a mild delamination route with LiF/HCl, which is conducive to loading the Bi_2MoO_6 nanoplates. The prepared MXene has a lateral size of 1–3 μm (Fig. 2a) with a thickness below 1.83 nm, indicating 1 or 2 layers on a substrate (Fig. S2). The Bi_2MoO_6 nanoplates were synthesized from $Bi(NO_3)_3{\cdot}5H_2O$ and $(NH_4)_6Mo_7O_{24}{\cdot}4H_2O$ via a hydrothermal method, leading to the presence of amino group on the surface of Bi_2MoO_6 nanoplates and thus positively charged. The synthesized Bi_2MoO_6 displays irregular plate-like morphology (Figs. 2b, S3a, b) with a lattice spacing of 0.277 nm, corresponding to the (200) plane of orthorhombic Bi_2MoO_6 (Fig. S3c) [31]. Its structure was further confirmed by the EDS mappings, which show a rough proportion of Bi, Mo, and O elements, coupled with the uniform distribution (Fig. S4). The Bi_2MoO_6 crystal structure intrinsically consisting of alternate $[Bi_2O_2]^{2+}$ layers and $[MoO_4]^{2-}$ perovskite layers offers open and stable channels for Li^+ insertion/extraction, endowing Bi_2MoO_6 with greatly improved rate capability compared with other TMOs. However, the intrinsic low conductivity and the large volume change during lithiation/delithiation of Bi_2MoO_6 still require the modification with conductive materials [28, 30]. The assembly of the Bi_2MoO_6 nanoplates with the $Ti_3C_2T_x$ MXene nanosheets was achieved by adding the Bi_2MoO_6 dispersion into the MXene solution and mixing thoroughly under continuous stirring. In order to confirm the successful electrostatic self-assembly of the Bi_2MoO_6/MXene heterostructure, the zeta potentials of the as-prepared heterostructures coupled with the two components, i.e., the pristine $Ti_3C_2T_x$ nanosheets and the Bi_2MoO_6 nanoplates, were measured. As shown in Fig. S5, the as-prepared MXene nanosheets are negatively charged with a zeta potential of −40.5 mV, which is ascribed to the presence of surface functional groups (e.g., –O, –F, and –OH) [32, 33]. When the positive-charged Bi_2MoO_6 (10.1 mV) mixed with the negative-charged MXene, Bi_2MoO_6 nanoplates were anchored on the MXene nanosheets based on an electrostatic interaction. Therefore, the zeta potentials of the Bi_2MoO_6/MXene heterostructures shift down with the increase in the MXene content, demonstrating the effective electrostatic process. In the assembled heterostructure, the highly conductive MXene nanosheets are expected to significantly enhance the conductivity and alleviate the volume expansion/contraction of Bi_2MoO_6 during lithiation/delithiation, thus improving the rate performance and cycling stability.

The morphologies of the Bi_2MoO_6/MXene heterostructures are shown in Fig. 2c–h. The composite samples were named with the mass ratio of Bi_2MoO_6/MXene: 50:50 (Bi_2MoO_6/MXene-50%, Fig. 2c, d), 70:30 (Bi_2MoO_6/MXene-30%, Fig. 2e, f), and 90:10 (Bi_2MoO_6/MXene-10%, Fig. 2g, h). It is apparent that with increasing Bi_2MoO_6 content, more Bi_2MoO_6 nanoplates cover on

the MXene nanosheets. For the Bi_2MoO_6/MXene-50%, the Bi_2MoO_6 nanoplates are sparsely wrapped with the MXene nanosheets (Fig. 2c, d). When the Bi_2MoO_6/MXene mass ratio increases to 70:30, the uniform and dense distribution of Bi_2MoO_6 is observed, almost covering the entire surface of the MXene nanosheets (Fig. 2e, f), implying an optimized mass ratio. As the Bi_2MoO_6 content continues to rise to 90 wt%, the Bi_2MoO_6 nanoplates evidently aggregate, as the insufficient surface area of the MXene nanosheets cannot load and anchor so many Bi_2MoO_6 nanoplates (Fig. 2g, h). TEM images were employed to further observe the structures of the Bi_2MoO_6/MXene heterostructures. It can be seen that the Bi_2MoO_6 nanoplates anchored on the MXene nanosheets have an irregular structure. The Bi_2MoO_6/MXene-50% (Fig. 3a, b), Bi_2MoO_6/MXene-30% (Fig. 3c, d), and Bi_2MoO_6/MXene-10% (Fig. 3e, f) display sparse, moderate, and dense distribution of Bi_2MoO_6 on the MXene nanosheets, respectively, in accordance with the corresponding SEM images. The STEM and corresponding element mappings (Fig. 3f) reveal similar images of Bi, Mo, Ti, and C elements, demonstrating the homogeneous distribution of Bi_2MoO_6 in the composite Bi_2MoO_6/MXene-30%.

XRD analysis was conducted to identify the composition of the samples, as shown in Fig. 4a. The XRD pattern of the as-prepared Bi_2MoO_6 nanoplates consists of strong (020) peak at 10.9° and (131) peak at 28.2° as well as several weak peaks corresponding to the (200), (060), (151), (202), and (062) planes of pristine Bi_2MoO_6 [49–51]. After the assembly process, the (002) peak of MXene occurs in the patterns of the composites, indicating the successful combination of Bi_2MoO_6 and MXene. Moreover, Fig. 4b displays the regional XRD profiles of the Bi_2MoO_6/MXene-10%, Bi_2MoO_6/MXene-30%, Bi_2MoO_6/MXene-50%, and pristine MXene, which is marked by a purple frame in Fig. 4a. The (002) peak of MXene downshifts as the mass ratio of the MXene decreases in the composites, which is attributed to the gradually increased lattice spacing of MXene expanded by the Bi_2MoO_6 nanoplates. The structures of

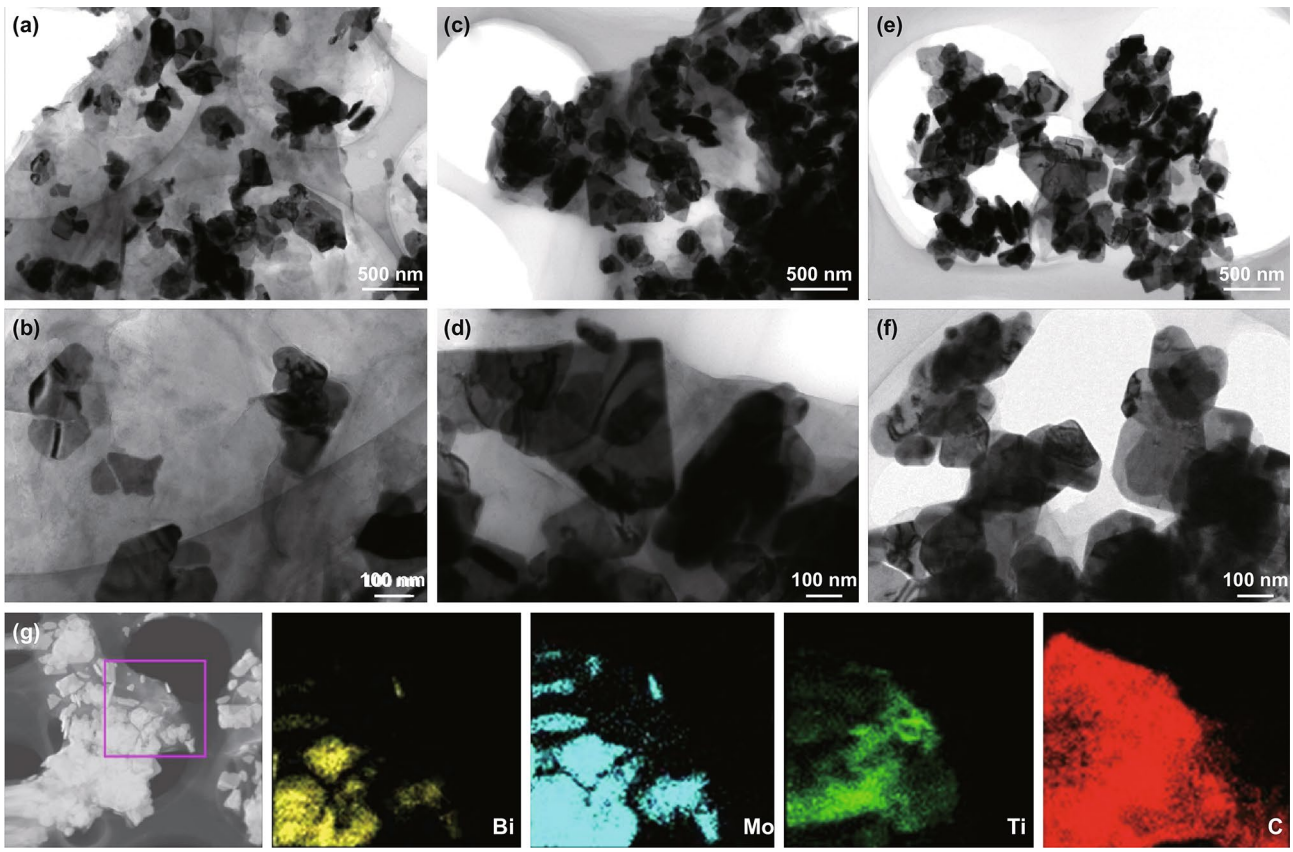

Fig. 3 TEM images of **a**, **b** Bi_2MoO_6/MXene-50%, **c**, **d** Bi_2MoO_6/MXene-30%, and **e**, **f** Bi_2MoO_6/MXene-10%. **g** STEM and corresponding element (Bi, Mo, Ti, and C) mapping images of the Bi_2MoO_6/MXene-30%

https://doi.org/10.1007/s40820-019-0312-y

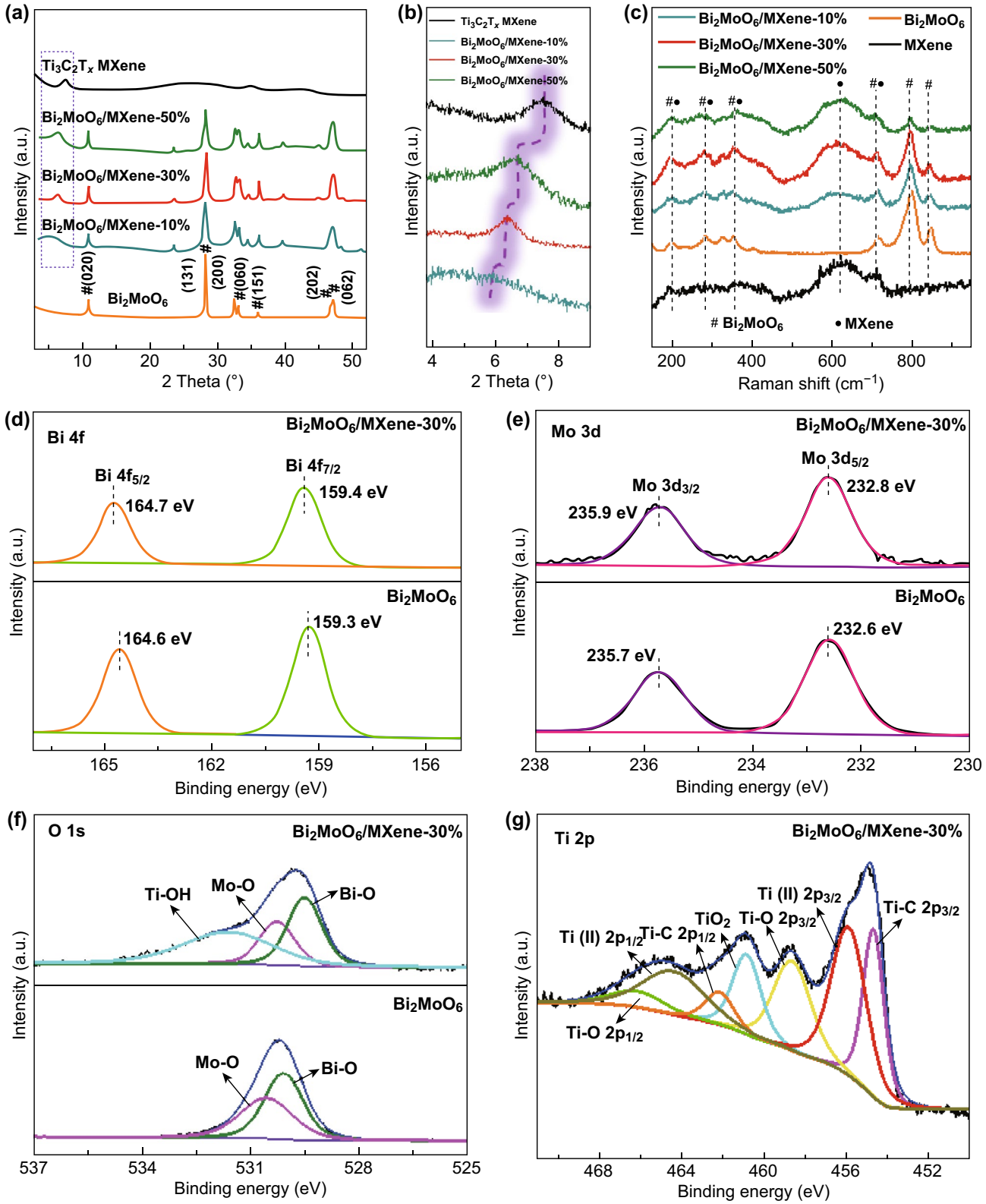

Fig. 4 Characterization of Bi_2MoO_6/MXene heterostructures: **a**, **b** XRD patterns, **c** Raman speatra of the Bi_2MoO_6/MXene heterostructures. High-resolution of **d** Bi 4*f*, **e** Mo 3*d*, **f** O 1*s*, and **g** Ti 2*p* XPS spectrum of Bi_2MoO_6/MXene-30%

the Bi_2MoO_6/MXene heterostructures were also characterized by Raman spectroscopy, and the results are shown in Fig. 4c. The pristine Bi_2MoO_6 displays distinct phonon modes in the range of 200–1000 cm^{-1}, signifying the vibrational modes of orthorhombic Bi_2MoO_6. Specifically, the bands located at 202, 285, 324, 355, and 404 cm^{-1} can be ascribed to the bending, wagging, and twisting modes of Mo–O bonds, while the bands at 713, 796, and 848 cm^{-1} correspond to the stretching modes of Mo–O bond [28, 31]. Notably, besides the band situated at 621 cm^{-1} (ω_4) corresponding to E_g in-plane vibration of surface functional group atoms, the bands of the pristine MXene show similar locations to the Bi_2MoO_6, including the bands located at 193 cm^{-1} (ω_2) and 711 cm^{-1} (ω_3) for A 1 g symmetry out-plane vibrations of Ti and C atoms and those at 284 cm^{-1} (ω_5) and 356 cm^{-1} (ω_5) for *E*g in-plane vibration of Ti and C atoms [52, 53]. The Bi_2MoO_6/MXene heterostructures display all the characteristic peaks belonging to Bi_2MoO_6 (e.g., 713, 796, and 848 cm^{-1}) and MXene (621 cm^{-1}), and the increase in MXene content in the heterostructures leads to the stronger peaks for MXene together with the weaker peaks for Bi_2MoO_6.

XPS was carried out to evaluate the surface chemical properties of the Bi_2MoO_6 nanoplates, pristine MXene, and Bi_2MoO_6/MXene-30%. The XPS survey of the Bi_2MoO_6/MXene-30% comprises the characteristic peaks of Bi_2MoO_6 and MXene, such as Ti 2*p* peak for $Ti_3C_2T_x$ as well as Bi 4*f* and Mo 3*d* peaks for Bi_2MoO_6 (Fig. S6), confirming the strong integration between the Bi_2MoO_6 nanoplates and the MXene nanosheets. High-resolution XPS spectra of Bi 4*f* and Mo 3*d* core levels of Bi_2MoO_6/MXene-30% and Bi_2MoO_6 are shown in Fig. 4d, e. The Bi 4*f* core level of Bi_2MoO_6/MXene-30% displays two peaks at 159.4 and 164.7 eV, related to Bi $4f_{7/2}$ and Bi $4f_{5/2}$ of the Bi^{3+}, respectively. Meanwhile, the Mo 3*d* core level of Bi_2MoO_6/MXene-30% could be divided into two peaks situated at 232.8 and 235.9 eV, which can be assigned to Mo $3d_{5/2}$ and Mo $3d_{3/2}$ of Mo^{6+}, respectively. It is noteworthy that the peaks of Bi 4*f* and Mo 3*d* core levels of Bi_2MoO_6/MXene-30% have higher binding energies than those of the Bi_2MoO_6, implying that the Bi_2MoO_6 nanoplates become more electrochemically active with the assistance of MXene. As shown in Fig. 4f, the O 1*s* core level of Bi_2MoO_6 is fitted with two components centered at 529.5 and 530.3 eV, which could be ascribed to Bi–O and Mo–O bonds, respectively [30, 47, 48]. Different from the Bi_2MoO_6, the Bi_2MoO_6/MXene-30% shows an additional peak at 531.6 eV corresponding to Ti–OH bond due to the presence of the MXene. Ti 2*p* XPS spectra are also showed in Fig. 4g to identify the chemical composition of the MXene. The Ti 2*p* core level was fitted with seven components, including three doublets (Ti $2p_{3/2}$–Ti $2p_{1/2}$) and a single peak located at 460.8 eV. The three doublets centered at 454.7/462.2, 455.9/464.4, and 458.7/466.1 eV could be assigned to Ti–C, Ti(II), and Ti–O, respectively, while the single peak might result from TiO_2, implying the partial oxidation of the MXene during the construction of the Bi_2MoO_6/MXene heterostructure [40, 50].

The lithium-ion storage behaviors of the Bi_2MoO_6/MXene composite electrodes and the Bi_2MoO_6 electrode were first explored by cyclic voltammetry (CV) for the first three cycles at a scan rate of 0.1 mV s^{-1} within a voltage range of 0.01–3 V, as shown in Fig. 5a and S7. All the electrodes show irreversible peaks at around 1.65, 1.26, and 0.58 V in the first cathodic scan, which could be attributed to the insertion of Li^+ into layer structure of the Bi_2MoO_6 crystal, the irreversible transformation from Bi_2MoO_6 to Bi and Mo metal (Eq. 2), the electrolyte decomposition, and formation of solid electrolyte interface (SEI) coupled with the alloying transformation from Bi to Li_3Bi, respectively [29–31]. Especially, the board peak at 0.58 V was subsequently split into several minor peaks, corresponding to the lithiation process of Bi to LiBi (Eq. 3) and Li_3Bi (Eq. 4). In the anodic scan, a strong peak at 0.98 V was observed which is caused by the de-alloying reaction of Li_3Bi. Besides, several board peaks at 1.31, 1.63, and 2.36 V are related to the oxidation of Mo (Eq. 5) and Bi (Eq. 6), respectively [28, 31]. The electrochemical reactions of the Bi_2MoO_6 are listed as follows:

$$Bi_2MoO_6 + 12Li^+ + 12e^- \rightarrow 2Bi + Mo + 6Li_2O \quad (2)$$

$$Bi + Li^+ + e^- \leftrightarrow LiBi \quad (3)$$

$$LiBi + 2Li^+ + 3e^- \leftrightarrow Li_3Bi \quad (4)$$

$$2Bi + 3Li_2O \leftrightarrow Bi_2O_3 + 6Li^+ + 6e^- \quad (5)$$

$$Mo + xLi_2O \leftrightarrow MoO_x + 2xLi^+ + 2xe^- \quad (x = 2, 3) \quad (6)$$

The galvanostatic charge/discharge curves of the electrodes were conducted at a current density of 100 mA g^{-1} in the voltage range of 0.01–3 V (Figs. 5b and S8), which show the electrochemical behaviors in accordance with the CV curves. The initial charge and discharge capacity of Bi_2MoO_6/MXene-30% is 615.5 and 844.2 mAh g^{-1},

 https://doi.org/10.1007/s40820-019-0312-y

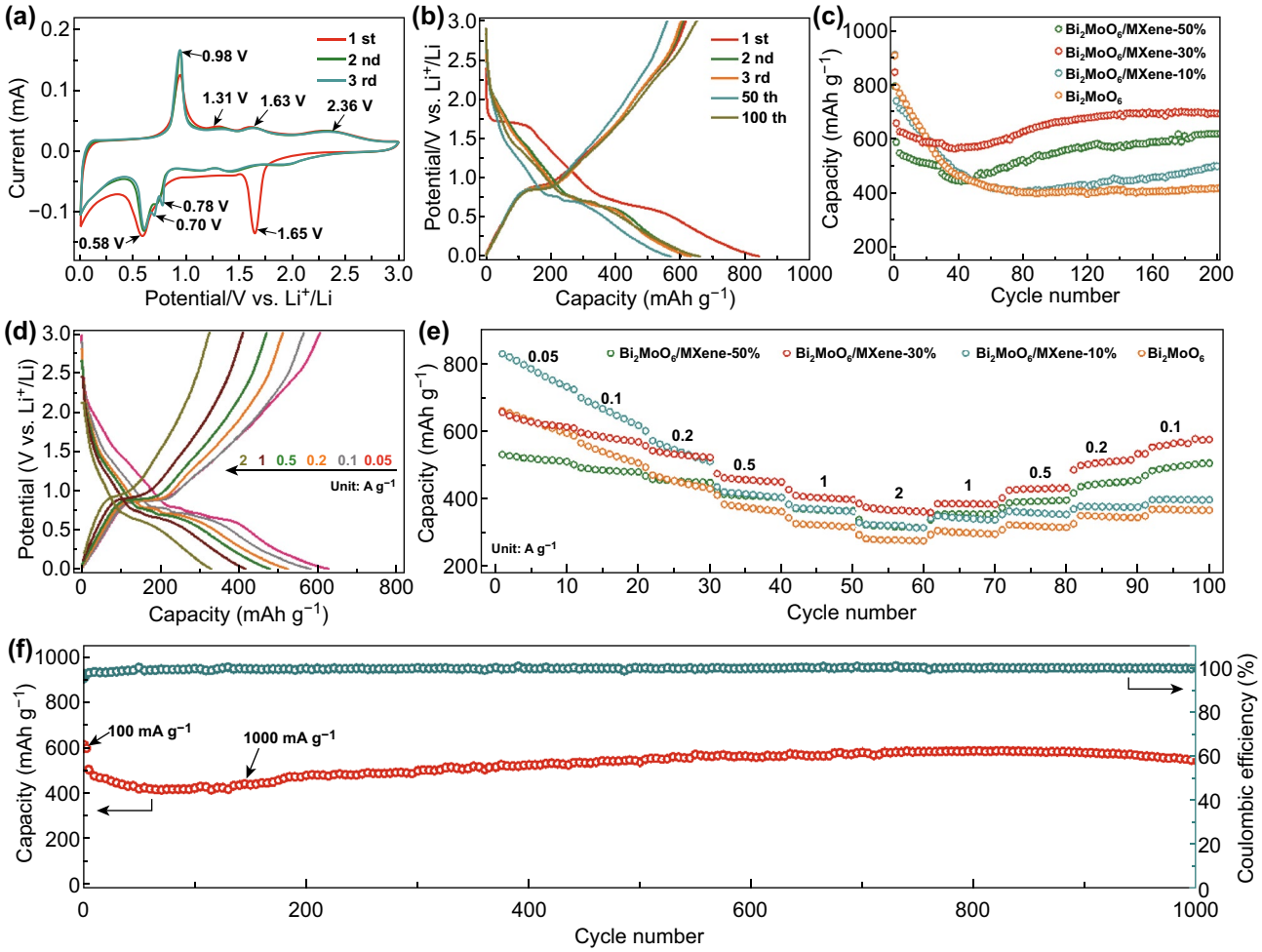

Fig. 5 Electrochemical performance of the Bi_2MoO_6/MXene electrodes: **a** CV curves of Bi_2MoO_6/MXene-30% for the first three cycles at 0.1 mV s^{-1}. **b** Charge/discharge profiles of Bi_2MoO_6/MXene-30% at 100 mA g^{-1} at different cycles. **c** Cycling performance of Bi_2MoO_6/MXene-50%, Bi_2MoO_6/MXene-30%, Bi_2MoO_6/MXene-10%, and pristine Bi_2MoO_6 electrodes at 100 mA g^{-1} for 200 cycles. **d** Charge/discharge profiles of Bi_2MoO_6/MXene-30% at different current rates. **e** Comparison of rate capabilities of Bi_2MoO_6/MXene-30% at various current rates from 50 to 2000 mA g^{-1}. **f** Long-term cycling performance of Bi_2MoO_6/MXene-30% in 1000 cycles at 1 A g^{-1}

respectively, leading to an initial coulombic efficiency (ICE) of 72.9%. The capacity loss in the first cycle might be attributed to the formation of SEI layer coupled with the irreversible reactions as mentioned above [31, 54, 55]. The ICE of Bi_2MoO_6/MXene-30% (72.9%) is lower than those of Bi_2MoO_6/MXene-10% (76.6%) and Bi_2MoO_6 (82.6%), but higher than that of Bi_2MoO_6/MXene-50% (71.2%). The possible reason for this phenomenon is that with higher MXene content, the increased surface area of MXene results in more irreversible reactions between Li^+ and the functional groups on the MXene surface, such as –O, –F, and –OH [47, 56].

The comparison of the cycling performance of the Bi_2MoO_6/MXene composite electrodes and the Bi_2MoO_6 electrode is given in Fig. 5c at a current density of 100 mA g^{-1}. The Bi_2MoO_6/MXene-30% delivers a stable capacity of 692 mAh g^{-1} after 200 cycles, much higher than those of Bi_2MoO_6/MXene-50% (617.5 mAh g^{-1}), Bi_2MoO_6/MXene-10% (497.6 mAh g^{-1}), and the pristine Bi_2MoO_6 (416.1 mAh g^{-1}). It indicates that the optimized ratio of the composite is beneficial for maximizing the lithium storage capacity of the Bi_2MoO_6/MXene. Furthermore, a capacity fading occurs in the initial dozens of cycles followed by a capacity reactivation process and an eventual capacity stabilization. The capacity fading results from the mechanical degradation of the electrode structure and the formation of an unstable SEI layer, while the subsequent capacity reactivation and stabilization could be ascribed to a restructuring process as well as stable SEI formation with cycling [57].

Figures 5d and S9 show the charge/discharge curves of Bi_2MoO_6/MXene-30% and the pristine Bi_2MoO_6 at various current densities from 0.05 to 2 A g^{-1}. As seen, the pristine Bi_2MoO_6 has a slightly higher capacity of 629.4 mAh g^{-1} at the small current density while it could only deliver capacities of 375.6, 323.7, and 279.8 mAh g^{-1} at 0.5, 1, and 2 A g^{-1}, respectively. By contrast, the specific capacity of Bi_2MoO_6/MXene-30% is measured to be 626.5, 580.6, 522.1, 477, 414.8, and 328.2 mAh g^{-1} at 0.05, 0.1, 0.2, 0.5, 1, and 2 A g^{-1}, respectively. It demonstrates that the conductive MXene effectively enhances the rate performance of the composite electrode. As displayed in Fig. 5e, the Bi_2MoO_6/MXene-30% exhibits the best rate capability from 0.05 to 2 A g^{-1} compared with the Bi_2MoO_6/MXene-50%, Bi_2MoO_6/MXene-10%, and Bi_2MoO_6 electrodes. When the current density is turned back from 2 to 0.1 A g^{-1}, the specific capacity of Bi_2MoO_6/MXene-30% are recovered up to 566.3 mAh g^{-1}, signifying the best reversibility and structural stability compared with other electrodes. Furthermore, to estimate the long-term cycling stability, Bi_2MoO_6/MXene-30% was charged/discharged for 1000 cycles at a high current density of 1 A g^{-1} (Fig. 5f). After the first three cycles at 0.1 A g^{-1} for activation, the Bi_2MoO_6/MXene-30% exhibits a reversible capacity of 507.2 mAh g^{-1} at the fifth cycle and retains a capacity of 545.1 mAh g^{-1} with 99.6% coulombic efficiency after 1000 cycles. The delivered capacity of Bi_2MoO_6/MXene-30% gradually increases with cycling, which is caused by the restructuring process and the subsequent formation of a stable structure during repeated lithiation/delithiation [57]. The SEM images of Bi_2MoO_6/MXene-30% before and after 1000 cycles at 1 A g^{-1} were explored to show the structural stability of the electrode as displayed in Fig. S10. It could be clearly seen that the Bi_2MoO_6 was wrapped by the MXene nanosheets, which are consistent with the SEM images of the Bi_2MoO_6/MXene-30% materials (Fig. 2e, f). After 1000 charge/discharge cycles, the surface of the electrode turns rough, but no obvious crack was observed, indicating the excellent structural stability of the Bi_2MoO_6/MXene-30% electrode during lithiation/delithiation.

To study the origins of the better rate capability of Bi_2MoO_6/MXene-30%, the lithium diffusion coefficients of Bi_2MoO_6/MXene-30% and Bi_2MoO_6 were calculated by GITT according to Eq. 1, as shown in Figs. 6a, b and

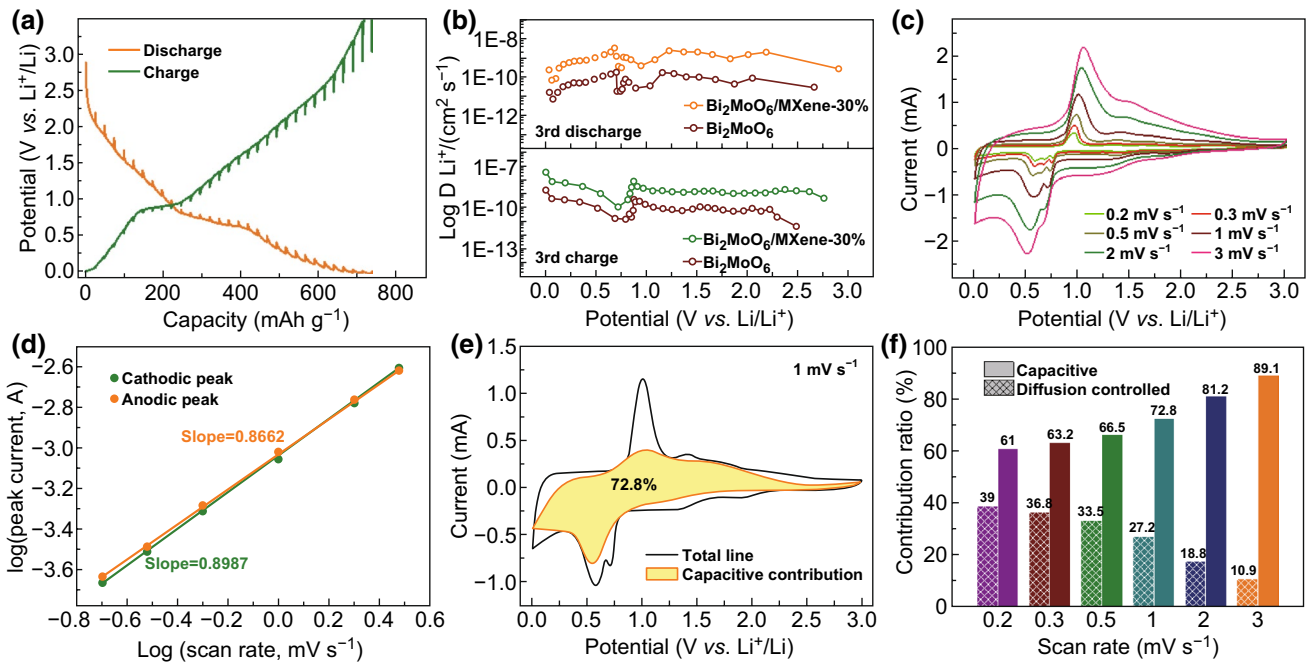

Fig. 6 Electrochemical kinetic analysis of Li storage behavior of Bi_2MoO_6/MXene-30%. **a** GITT profiles (current pulse at 100 mA g^{-1} for 30 min followed by 1 h relaxation), **b** diffusion coefficients calculated from GITT profiles according to overpotential, **c** CV curves at various scan rates from 0.2 to 3 mV s^{-1} in the voltage range of 0.01–3 V (vs. Li^+/Li), **d** log(*i*)–log(*v*) curves, **e** CV profile measured at 1 mV s^{-1} with shaded area displaying the pseudocapacitive contribution, and **f** normalized proportions of capacitive and diffusion-controlled contribution at various scan rates

https://doi.org/10.1007/s40820-019-0312-y

S10. Compared with the Bi_2MoO_6, Bi_2MoO_6/MXene-30% exhibits lower overpotential and higher diffusion coefficients during the lithiation/delithiation process, implying better reaction kinetics [58, 59]. The enhanced reaction kinetics of Bi_2MoO_6/MXene-30% can be associated with the decoration of the highly conductive MXene nanosheets, which support and contact with the Bi_2MoO_6 nanoplates sufficiently to efficiently improve the charge transport. Additionally, the EIS spectra show that the Bi_2MoO_6/MXene-30% has the lowest R_{ct} resistance of 105.9 Ω and R_s resistance of 3.08 Ω among these four samples, verifying its enhanced reaction kinetics for lithium-ion storage (Fig. S12a, b, Table S1). The impedance behaviors of the Bi_2MoO_6/MXene-30% and Bi_2MoO_6 electrodes were explored by the complex model of capacity to confirm the promotion of MXene for rapid diffusion and transportation of lithium ions (Fig. S12c, d). After the decoration of MXene, the Bi_2MoO_6/MXene-30% displays much lower minimal characteristic relaxation time constant τ_0 (919 ms) and downtrend of normalized $C'(\omega)$ than the pristine Bi_2MoO_6 electrodes, implying faster transport and diffusion of electrolyte ions in the Bi_2MoO_6/MXene-30% electrode [52].

CV measurements were taken to unravel the charge storage kinetics of Bi_2MoO_6/MXene-30%. Figure 6a depicts the CV curves of Bi_2MoO_6/MXene-30% at various scan rates from 0.2 to 3 mV s^{-1}. The charge storage mechanism could be analyzed by the following formula, which shows the relationship between the measured current (i) and the scan rate (v):

$$i = av^b \tag{7}$$

where b could be calculated from the slope of the fitted $\log(i) - \log(v)$ curves [60, 61], distinguishing the electrochemical behavior as a diffusion-controlled process ($b = 0.5$) or a non-diffusion-controlled behavior ($b = 1$). As shown in Fig. 6d, the b value of Bi_2MoO_6/MXene-30% is 0.8987 at 0.58 V in the cathodic scan and 0.8662 at 0.97 V in the anodic scan, indicating a fast charge storage kinetic dominated by pseudocapacitive behavior. This behavior can also be confirmed by quantifying the pseudocapacitive contribution based on Eq. 8:

$$i(v) = k_1 v + k_2 v^{1/2} \tag{8}$$

where $i(v)$, $k_1 v$, $k_2 v^{1/2}$, and v are the measured current at a certain potential, the capacitive-dominated current, the diffusion-controlled current, and the corresponding scan rate, respectively. The capacitive-dominated current at a certain scan rate could be obtained via calculating the value of k_1 [60, 61]. Figures 6e and S13 depict the CV curves of Bi_2MoO_6/MXene-30% at various scan rates, in which the shaded portion stands for the capacitive-dominated region, while the non-shaped portion means the diffusion-controlled region. It can be seen that up to 72.8% of the charge is contributed by the pseudocapacitive behavior at 1 mV s^{-1}. Moreover, the pseudocapacitive contribution of the Bi_2MoO_6/MXene-30% electrode enhances with the scan rate increasing (Fig. 6f). The capacitive-dominated mechanism coupled with the highly conductive MXene can offer ultrafast lithium-ion storage, endowing Bi_2MoO_6/MXene-30% with enhanced rate capability and cycling stability.

The above results suggest that the lithium storage property of Bi_2MoO_6 could be effectively enhanced by introducing highly conductive MXene as a substrate to fabricate a plate-to-layer Bi_2MoO_6/MXene heterostructure. In the heterostructure, the MXene nanosheets can promote the charge transport and alleviate the volume change of the Bi_2MoO_6, leading to high specific capacity, superior rate capability, and excellent long-term cycling stability. The Bi_2MoO_6/MXene-30% exhibits competitive performance compared with other TMOs-based electrodes, indicating its promising potential as an anode material of LIBs.

4 Conclusions

To solve the problems of Bi_2MoO_6 as an electrode material for LIBs, i.e., low electronic conductivity and huge volume change, we have fabricated Bi_2MoO_6 nanoplates on highly conductive $Ti_3C_2T_x$ MXene nanosheets to form a plate-to-layer heterostructure via a simple electrostatic self-assembled method. In the Bi_2MoO_6/MXene heterostructure, the MXene nanosheets cannot only promote the electron transfer and facilitate the Li^+ transport, but also accommodate the volume expansion/contraction of Bi_2MoO_6 during lithiation/delithiation, endowing the composite electrodes with high conductivity, good structural stability, and excellent electrochemical durability. As a result, the Bi_2MoO_6/MXene-30% exhibits remarkably enhanced lithium storage properties, presenting a specific capacity of 692 mAh g^{-1} at 100 mA g^{-1} after 200 cycles, a superior rate capability of 328.2 mAh g^{-1} at 2 A g^{-1} as well as an outstanding cycling durability with a capacity of 545.1 mAh g^{-1} and 99.6% coulombic efficiency at 1 A g^{-1} after 1000 cycles. The Bi_2MoO_6/MXene heterostructure with competitive performance is conceivable to be a promising high-performance anode material for LIBs.

Furthermore, various TMOs/$Ti_3C_2T_x$ composites were suggested to be explored using $Ti_3C_2T_x$ MXene nanosheets as a conductive substrate to achieve good electrochemical performance and application in energy storage.

Acknowledgements This work was financially supported by the National Natural Science Foundation of China (Nos. 51572011 and 51802012) and the National Key Research and Development Program of China (2017YFB0102204).

Electronic supplementary material The online version of this article (https://doi.org/10.1007/s40820-019-0312-y) contains supplementary material, which is available to authorized users.

References

1. S. Niu, Z. Wang, M. Yu, M. Yu, L. Xiu, S. Wang, X. Wu, J. Qiu, MXene-based electrode with enhanced pseudocapacitance and volumetric capacity for power-type and ultra-long life lithium storage. ACS Nano **12**, 3928–3937 (2018). https://doi.org/10.1021/acsnano.8b01459
2. Y. Zhong, B. Li, S. Li, S. Xu, Z. Pan et al., Bi nanoparticles anchored in N-doped porous carbon as anode of high energy density lithium ion battery. Nano-Micro Lett. **10**, 56 (2018). https://doi.org/10.1007/s40820-018-0209-1
3. N. Sun, Z. Guan, Y. Liu, Y. Cao, Q. Zhu et al., Extended "adsorption–insertion" model: a new insight into the sodium storage mechanism of hard carbons. Adv. Energy Mater. **9**, 1901351 (2019). https://doi.org/10.1002/aenm.201901351
4. Y. Huang, H. Yang, Y. Zhang, Y. Zhang, Y. Wu et al., A safe and fast-charging lithium-ion battery anode using MXene supported Li_3VO_4. J. Mater. Chem. A **7**, 11250–11256 (2019). https://doi.org/10.1039/c9ta02037c
5. Q. Xu, J.-K. Sun, Y.-X. Yin, Y.-G. Guo, Facile synthesis of blocky SiO_x/C with graphite-like structure for high-performance lithium-ion battery anodes. Adv. Funct. Mater. **28**, 1705235 (2018). https://doi.org/10.1002/adfm.201705235
6. H. Tabassum, R. Zou, A. Mahmood, Z. Liang, Q. Wang et al., A universal strategy for hollow metal oxide nanoparticles encapsulated into B/N Co-doped graphitic nanotubes as high-performance lithium-ion battery anodes. Adv. Mater. **30**, 1705441 (2018). https://doi.org/10.1002/adma.201705441
7. M. Zheng, H. Tang, L. Li, Q. Hu, L. Zhang, H. Xue, H. Pang, Hierarchically nanostructured transition metal oxides for lithium-ion batteries. Adv. Sci. **5**, 1700592 (2018). https://doi.org/10.1002/advs.201700592
8. S.H. Yu, S.H. Lee, D.J. Lee, Y.E. Sung, T. Hyeon, Conversion reaction-based oxide nanomaterials for lithium ion battery anodes. Small **12**, 2146–2172 (2016). https://doi.org/10.1002/smll.201502299
9. J. Zhang, H. Ren, J. Wang, J. Qi, R. Yu, D. Wang, Y. Liu, Engineering of multi-shelled SnO_2 hollow microspheres for highly stable lithium-ion batteries. J. Mater. Chem. A **4**, 17673–17677 (2016). https://doi.org/10.1039/c6ta07717j
10. M.S. Park, G.X. Wang, Y.M. Kang, D. Wexler, S.X. Dou, H.K. Liu, Preparation and electrochemical properties of SnO_2 nanowires for application in lithium-ion batteries. Angew. Chem. Int. Ed. **46**, 750–753 (2007). https://doi.org/10.1002/anie.200603309
11. H. Liu, M. Jia, Q. Zhu, B. Cao, R. Chen et al., 3D-0D graphene-Fe_3O_4 quantum dot hybrids as high-performance anode materials for sodium-ion batteries. ACS Appl. Mater. Interfaces **8**, 26878–26885 (2016). https://doi.org/10.1021/acsami.6b09496
12. M. Wang, Y. Huang, N. Zhang, K. Wang, X. Chen, X. Ding, A facile synthesis of controlled Mn_3O_4 hollow polyhedron for high-performance lithium-ion battery anodes. Chem. Eng. J. **334**, 2383–2391 (2018). https://doi.org/10.1016/j.cej.2017.12.017
13. M.V. Reddy, G.V. Subba Rao, B.V.R. Chowdari, Metal oxides and oxysalts as anode materials for li ion batteries. Chem. Rev. **113**, 5364–5457 (2013). https://doi.org/10.1021/cr3001884
14. Y. Lu, L. Yu, X.W. Lou, Nanostructured conversion-type anode materials for advanced lithium-ion batteries. Chem **4**, 972–996 (2018). https://doi.org/10.1016/j.chempr.2018.01.003
15. W.J. Zhang, A review of the electrochemical performance of alloy anodes for lithium-ion batteries. J. Power Sources **196**, 12–24 (2011). https://doi.org/10.1016/j.jpowsour.2010.07.020
16. N. Mahmood, T. Tang, Y. Hou, Nanostructured anode materials for lithium ion batteries: progress, challenge and perspective. Adv. Energy Mater. **6**, 1600374 (2016). https://doi.org/10.1002/aenm.201600374
17. J.S. Chen, X.W. Lou, SnO_2-based nanomaterials: synthesis and application in lithium-ion batteries. Small **9**, 1877–1893 (2013). https://doi.org/10.1002/smll.201202601
18. C. Kim, J.W. Jung, K.R. Yoon, D.Y. Youn, S. Park, I.D. Kim, A high-capacity and long-cycle-life lithium-ion battery anode architecture: silver nanoparticle-decorated SnO_2/NiO Nanotubes. ACS Nano **10**, 11317–11326 (2016). https://doi.org/10.1021/acsnano.6b06512
19. Y. Lu, J. Nai, X.W. Lou, Formation of $NiCo_2V_2O_8$ yolk–double shell spheres with enhanced lithium storage properties. Angew. Chem. Int. Ed. **57**, 2899–2903 (2018). https://doi.org/10.1002/anie.201800363
20. Y. Zhang, K. Zhang, S. Ren, K. Jia, Y. Dang et al., 3D nanoflower-like composite anode of α-Fe_2O_3/coal-based graphene for lithium-ion batteries. J. Alloy Compd. **792**, 828–834 (2019). https://doi.org/10.1016/j.jallcom.2019.04.011

21. K. Yu, X. Pan, G. Zhang, X. Liao, X. Zhou, M. Yan, L. Xu, L. Mai, Nanowires in energy storage devices: structures, synthesis, and applications. Adv. Energy Mater. **8**, 1802369 (2018). https://doi.org/10.1002/aenm.201802369
22. L. Yu, H. Hu, H.B. Wu, X.W. Lou, Complex hollow nanostructures: synthesis and energy-related applications. Adv. Mater. **29**, 1604563 (2017). https://doi.org/10.1002/adma.201604563
23. W. Chen, K. Song, L. Mi, X. Feng, J. Zhang, S. Cui, C. Liu, Synergistic effect induced ultrafine SnO_2/graphene nanocomposite as an advanced lithium/sodium-ion batteries anode. J. Mater. Chem. A **5**, 10027–10038 (2017). https://doi.org/10.1039/c7ta01634d
24. Y.M. Chen, L. Yu, X.W. Lou, Hierarchical tubular structures composed of Co_3O_4 hollow nanoparticles and carbon nanotubes for lithium storage. Angew. Chem. Int. Ed. **55**, 5990–5993 (2016). https://doi.org/10.1002/anie.201600133
25. Q. Tian, F. Zhang, L. Yang, Fabricating thin two-dimensional hollow tin dioxide/carbon nanocomposite for high-performance lithium-ion battery anode. Appl. Surf. Sci. **481**, 1377–1384 (2019). https://doi.org/10.1016/j.apsusc.2019.03.252
26. X. Yang, Y. Xiang, X. Wang, S. Li, H. Chen, X. Ding, Pyrene-based conjugated polymer/Bi_2MoO_6 Z-scheme hybrids: facile construction and sustainable enhanced photocatalytic performance in ciprofloxacin and Cr(VI) removal under visible light irradiation. Catalysis **8**, 185 (2018). https://doi.org/10.3390/catal8050185
27. W.-B. Chen, L.-N. Zhang, Z.-J. Ji, Y.-D. Zheng, S. Yuan, Q. Wang, Self-supported Bi_2MoO_6 nanosheet arrays as advanced integrated electrodes for Li-ion batteries with super high capacity and long cycle life. Nano **13**, 1850066 (2018). https://doi.org/10.1142/S1793292018500662
28. X. Zhai, J. Gao, R. Xue, X. Xu, L. Xu, L. Wang, Q. Tian, Y. Liu, Facile synthesis of Bi_2MoO_6/reduced graphene oxide composites as anode materials towards enhanced lithium storage performance. J. Colloid Interface Sci. **518**, 242–251 (2018). https://doi.org/10.1016/j.jcis.2018.02.012
29. S. Yuan, Y. Zhao, W. Chen, C. Wu, X. Wang, L. Zhang, Q. Wang, Self-assembled 3D hierarchical porous Bi_2MoO_6 microspheres toward high capacity and ultra-long-life anode material for li-ion batteries. ACS Appl. Mater. Interfaces **9**, 21781–21790 (2017). https://doi.org/10.1021/acsami.7b04045
30. Y. Zheng, T. Zhou, X. Zhao, W.K. Pang, H. Gao et al., Atomic interface engineering and electric-field effect in ultrathin Bi_2MoO_6 nanosheets for superior lithium ion storage. Adv. Mater. **29**, 1700396 (2017). https://doi.org/10.1002/adma.201700396
31. Y. Zhang, G. Zhao, P. Ge, T. Wu, L. Li et al., Bi_2MoO_6 microsphere with double-polyaniline layers toward ultrastable lithium energy storage by reinforced structure. Inorg. Chem. **58**, 6410–6421 (2019). https://doi.org/10.1021/acs.inorgchem.9b00627
32. A. Lipatov, M. Alhabeb, M.R. Lukatskaya, A. Boson, Y. Gogotsi, A. Sinitskii, Effect of synthesis on quality, electronic properties and environmental stability of individual monolayer Ti_3C_2 MXene flakes. Adv. Electron. Mater. **2**, 1600255 (2016). https://doi.org/10.1002/aelm.201600255
33. B. Anasori, M.R. Lukatskaya, Y. Gogotsi, 2D metal carbides and nitrides (MXenes) for energy storage. Nat. Rev. Mater. **2**, 16098 (2017). https://doi.org/10.1038/natrevmats.2016.98
34. L. Yu, L. Hu, B. Anasori, Y.-T. Liu, Q. Zhu, P. Zhang, Y. Gogotsi, B. Xu, MXene-bonded activated carbon as a flexible electrode for high-performance supercapacitors. ACS Energy Lett. **3**, 1597–1603 (2018). https://doi.org/10.1021/acsenergylett.8b00718
35. Y. Tian, Y. An, J. Feng, Flexible and freestanding silicon/MXene composite papers for high-performance lithium-ion batteries. ACS Appl. Mater. Interfaces **11**, 10004–10011 (2019). https://doi.org/10.1021/acsami.8b21893
36. Z. Lin, D. Sun, Q. Huang, J. Yang, M.W. Barsoum, X. Yan, Carbon nanofiber bridged two-dimensional titanium carbide as a superior anode for lithium-ion batteries. J. Mater. Chem. A **3**, 14096–14100 (2015). https://doi.org/10.1039/c5ta01855b
37. M. Xu, S. Lei, J. Qi, Q. Dou, L. Liu et al., Opening magnesium storage capability of two-dimensional MXene by intercalation of cationic surfactant. ACS Nano **12**, 3733–3740 (2018). https://doi.org/10.1021/acsnano.8b00959
38. Q. Tang, Z. Zhou, P. Shen, Are MXenes promising anode materials for Li ion batteries? Computational studies on electronic properties and Li storage capability of Ti_3C_2 and $Ti_3C_2X_2$ (X = F, OH) monolayer. J. Am. Chem. Soc. **134**, 16909–16916 (2012). https://doi.org/10.1021/ja308463r
39. Y. Tian, Y. An, S. Xiong, J. Feng, Y. Qian, A general method for constructing robust, flexible and freestanding MXene@metal anodes for high-performance potassium-ion batteries. J. Mater. Chem. A **7**, 9716–9725 (2019). https://doi.org/10.1039/c9ta02233c
40. Y.-T. Liu, P. Zhang, N. Sun, B. Anasori, Q.-Z. Zhu, H. Liu, Y. Gogotsi, B. Xu, Self-assembly of transition metal oxide nanostructures on MXene nanosheets for fast and stable lithium storage. Adv. Mater. **30**, 1707334 (2018). https://doi.org/10.1002/adma.201707334
41. H. Liu, X. Zhang, Y. Zhu, B. Cao, Q. Zhu et al., Electrostatic self-assembly of 0D–2D SnO_2 quantum dots/$Ti_3C_2T_x$ MXene hybrids as anode for lithium-ion batteries. Nano-Micro Lett. **11**(65), 65 (2019). https://doi.org/10.1007/s40820-019-0296-7
42. Y. Wang, Y. Li, Z. Qiu, X. Wu, P. Zhou et al., Fe_3O_4@Ti_3C_2 MXene hybrids with ultrahigh volumetric capacity as an anode material for lithium-ion batteries. J. Mater. Chem. A **6**, 11189–11197 (2018). https://doi.org/10.1039/c8ta00122g
43. X. Guo, X. Xie, S. Choi, Y. Zhao, H. Liu, C. Wang, S. Chang, G. Wang, Sb_2O_3/MXene($Ti_3C_2T_x$) hybrid anode materials with enhanced performance for sodium-ion batteries. J. Mater. Chem. A **5**, 12445–12452 (2017). https://doi.org/10.1039/c7ta02689g
44. C. Wei, H. Fei, Y. An, Y. Zhang, J. Feng, Crumpled $Ti_3C_2T_x$ (MXene) nanosheet encapsulated $LiMn_2O_4$ for high performance lithium-ion batteries. Electrochim. Acta **309**, 362–370 (2019). https://doi.org/10.1016/j.electacta.2019.04.094
45. M.-Q. Zhao, M. Torelli, C.E. Ren, M. Ghidiu, Z. Ling, B. Anasori, M.W. Barsoum, Y. Gogotsi, 2D titanium carbide and transition metal oxides hybrid electrodes for Li-ion storage. Nano Energy **30**, 603–613 (2016). https://doi.org/10.1016/j.nanoen.2016.10.062

46. Q. Zhao, Q. Zhu, J. Miao, P. Zhang, B. Xu, 2D MXene nanosheets enable small-sulfur electrodes to be flexible for lithium–sulfur batteries. Nanoscale **11**, 8442–8448 (2019). https://doi.org/10.1039/c8nr09653h
47. P. Zhang, Q. Zhu, Z. Guan, Q. Zhao, N. Sun, B. Xu, A Flexible Si@C Electrode with excellent stability employing an MXene as a multifunctional binder for lithium-ion batteries. ChemSusChem **12**, 1–9 (2019). https://doi.org/10.1002/cssc.201901497
48. J. Wu, Y. Sun, C. Gu, T. Wang, Y. Xin, C. Chai, C. Cui, D. Ma, Pt supported and carbon coated Bi_2MoO_6 composite for enhanced 2,4-dibromophenol degradation under visible–light irradiation: insight into band gap structure and photocatalytic mechanism. Appl. Catal. B: Environ. **237**, 622–632 (2018). https://doi.org/10.1016/j.apcatb.2018.06.016
49. X. Wang, T.S. Mathis, K. Li, Z. Lin, L. Vlcek et al., Influences from solvents on charge storage in titanium carbide MXenes. Nat. Energy **4**, 241–248 (2019). https://doi.org/10.1038/s41560-019-0339-9
50. H. Shen, W. Xue, F. Fu, J. Sun, Y. Zhen, D. Wang, B. Shao, J. Tang, Efficient degradation of phenol and 4-nitrophenol by surface oxygen vacancies and plasmonic silver Co-modified Bi_2MoO_6 photocatalysts. Chem. Eur. J. **24**, 18463–18478 (2018). https://doi.org/10.1002/chem.201804267
51. L. Guo, Q. Zhao, H. Shen, X. Han, K. Zhang, D. Wang, F. Fu, B. Xu, Ultrafine Au nanoparticles anchored on Bi_2MoO_6 with abundant surface oxygen vacancies for efficient oxygen molecule activation. Catal. Sci. Technol. **9**, 3193–3202 (2019). https://doi.org/10.1039/c9cy00579j
52. J. Yan, C.E. Ren, K. Maleski, C.B. Hatter, B. Anasori, P. Urbankowski, A. Sarycheva, Y. Gogotsi, Flexible MXene/graphene films for ultrafast supercapacitors with outstanding volumetric capacitance. Adv. Funct. Mater. **27**, 1701264 (2017). https://doi.org/10.1002/adfm.201701264
53. L. Shen, X. Zhou, X. Zhang, Y. Zhang, Y. Liu, W. Wang, W. Si, X. Dong, Carbon-intercalated $Ti_3C_2T_x$ MXene for high-performance electrochemical energy storage. J. Mater. Chem. A **6**, 23513–23520 (2018). https://doi.org/10.1039/c8ta09600g
54. S. Nie, L. Liu, J. Liu, J. Xie, Y. Zhang et al., Nitrogen-doped TiO_2–C composite nanofibers with high-capacity and long-cycle life as anode materials for sodium-ion batteries. Nano-Micro Lett. **10**, 71 (2018). https://doi.org/10.1007/s40820-018-0225-1
55. N. Sun, H. Liu, Bin Xu, Facile synthesis of high performance hard carbon anode materials for sodium ion batteries. J. Mater. Chem. A **3**, 20560–20566 (2015). https://doi.org/10.1039/c5ta05118e
56. M.-Q. Zhao, X. Xie, C.E. Ren, T. Makaryan, B. Anasori, G. Wang, Y. Gogotsi, Hollow MXene spheres and 3D macroporous MXene frameworks for Na-ion storage. Adv. Mater. **29**, 1702410 (2017). https://doi.org/10.1002/adma.201702410
57. H. Sun, G. Xin, T. Hu, M. Yu, D. Shao, X. Sun, J. Lian, High-rate lithiation-induced reactivation of mesoporous hollow spheres for long-lived lithium-ion batteries. Nat. Commun. **5**, 4526 (2014). https://doi.org/10.1038/ncomms5526
58. B. Cao, Q. Zhang, H. Liu, B. Xu, S. Zhang et al., Graphitic carbon nanocage as a stable and high power anode for potassium-ion batteries. Adv. Energy Mater. **8**, 1801149 (2018). https://doi.org/10.1002/aenm.201801149
59. H. Liu, S. Zhang, Q. Zhu, B. Cao, P. Zhang et al., Fluffy carbon-coated red phosphorus as a highly stable and high-rate anode for lithium-ion batteries. J. Mater. Chem. A **7**, 11205–11213 (2019). https://doi.org/10.1039/c9ta02030f
60. R. Meng, J. Huang, Y. Feng, L. Zu, C. Peng et al., Black phosphorus quantum dot/Ti_3C_2 MXene nanosheet composites for efficient electrochemical lithium/sodium-ion storage. Adv. Energy Mater. **8**, 1801514 (2018). https://doi.org/10.1002/aenm.201801514
61. X. Guo, J. Zhang, J. Song, W. Wu, H. Liu, G. Wang, MXene encapsulated titanium oxide nanospheres for ultra-stable and fast sodium storage. Energy Storage Mater. **14**, 306–313 (2018). https://doi.org/10.1016/j.ensm.2018.05.010

 https://doi.org/10.1007/s40820-019-0312-y